Quasiparticle phono-conversion: filming carriers coalescing into excitons

Enrico Perfetto[1,2], Takumi Fukuda[3], Xing Zhu[3], Jacques Hawecker[3], Harley Suchiang[3], Joanna Nadolna[3,4], Nanami Tomoda[3], Suji Park[5], Houk Jang[5], Kenji Watanabe[6], Takashi Taniguchi[7], Michael K. L. Man[3], Julien Madéo[3], Keshav M. Dani[3], Gianluca Stefanucci[1,2]

[1]Dipartimento di Fisica, Università di Roma Tor Vergata, Via della Ricerca Scientifica 1, 00133 Rome, Italy.
[2]INFN, Sezione di Roma Tor Vergata, Via della Ricerca Scientifica 1, 00133 Rome, Italy.
[3]Femtosecond Spectroscopy Unit, Okinawa Institute of Science and Technology Graduate University, Onna, Okinawa, Japan 904-0495 .
[4]Laboratory of photocatalysis, Department of Environmental Technology, Faculty of Chemistry, University of Gdansk, 80–308 Gdansk, Poland .
[5]Center for Functional Nanomaterials, Brookhaven National Laboratory, Upton, New York 11973, USA .
[6] Research Center for Electronic and Optical Materials, National Institute for Materials Science, 1-1 Namiki, Tsukuba 305-0044, Japan .
[7]Research Center for Materials Nanoarchitectonics, National Institute for Materials Science, 1-1 Namiki, Tsukuba 305-0044, Japan .

Contributing authors: eperfett@roma2.infn.it; kmdani@oist.jp; stefanuc@roma2.infn.it;

Abstract

Condensed matter physics is replete with phenomena involving high-energy free particles coalescing into low-energy bound few-particle states. While the cooling of the individual particles is well understood, the crucial step by which cold free carriers form a bound state remains elusive, involving complex energy and momentum relaxation pathways. Here, by combining ultrafast time- and momentum-resolved photoemission spectroscopy on a monolayer WSe_2 with the

first-principles excitonic-Bloch equations, we resolve the conversion of initially free electrons and holes at the bandedges into bound excitons. With unprecedented energy resolution, we observe the transient *coexistence* of free-carrier and excitonic bands, accompanied by a transfer of spectral weight between the two. We establish the phononic origin of exciton formation and ascribe this coexistence to a sequential relaxation cascade toward the lowest-energy excitonic states, wherein intermediate states remain weakly populated. The efficiency of this process is controlled by valley multiplicity, large-momentum phonon emission and spin-flip processes. By elucidating how bound states emerge from their elementary constituents, our results point to strategies for engineering exciton formation, with direct implications for optical materials and devices that operate with excitons or free carriers.

Introduction

Exciton formation [1–8] lies at the core of light–matter interaction in 2D semiconductors, setting the fundamental limits for energy conversion and information processing [9–12]. The efficiency and speed with which excitons emerge determine how effectively these materials can power technologies such as solar cells, photodetectors, and quantum optoelectronic devices.

Excitons can form via two primary pathways [1]. The first is resonant (or direct) photoexcitation, in which photons with energies matching the exciton transition directly create excitons (Fig. 1a). This conceptually simple mechanism, well-captured by mean-field theories [13–16], has enabled the exploration of a wide array of emergent excitonic phenomena, including valley polarization [17, 18], exciton-driven Floquet physics [19, 20], exciton superfluidity [21], and bright-to-dark exciton scattering [22, 23].

By contrast, the second mechanism, non-resonant (or indirect) excitation, is significantly more complex. Here, high-energy photons promote electrons and holes far above their respective band edges, generating hot quasi-free carriers which subsequently cool toward the band extrema through phonon emission—a process that is relatively well understood [24, 25]. Exciton formation then occurs as electrons near the conduction band minimum and holes near the valence band maximum bind through a cascade of phonon-mediated scatterings constrained by energy- and momentum-conservation (Fig. 1b) [26]. Unraveling such a relaxation process is crucial for defining a fundamental timescale for hot carrier extraction before exciton formation in 2D material-based devices, thereby setting intrinsic efficiency limits for 2D-based optoelectronic technologies [27].

Despite its fundamental importance, the early-stage dynamics of exciton formation under non-resonant excitation remains largely inaccessible, and consequently far less understood. Experimental observations so far have been restricted to time-resolved optical spectroscopy signals that capture the consequences of exciton formation [4, 6–8, 28], rather than the excitons themselves. In fact, the population of excitons and

free carriers cannot be directly disentangled and are instead inferred from phenomenological two-component models [29, 30]. In principle, time- and angle-resolved photoemission spectroscopy (tr-ARPES) provides a direct route to track the conversion of free carriers into excitons with full momentum and energy resolution. However, experimental limitations have thus far hindered a direct and conclusive observation of this process [22, 31]. Compounding the experimental challenges, the theoretical modeling of this nonequilibrium dynamics is equally formidable. Unlike resonant excitation, where excitons are generated directly, nonresonant excitation defies simple theoretical treatment capable to describe the multistep evolution of the transient mixture of unbound carriers and bound excitons. Accurately describing this relaxation process requires demanding computational resources and the development of advanced many-body theoretical frameworks [32].

In this work, we directly observe the phonon-mediated coalescence of free electron–hole pairs into excitons in non-resonantly photoexcited monolayer (1L-) WSe_2. Using tr-ARPES experiments with unprecedented energy resolution (see Fig. 1c for schematic setup and "Methods" for details), we resolve the transient *coexistence* of free carriers and excitons during the conversion process. Immediately following photoexcitation, the tr-ARPES spectrum reveals the characteristic low-energy shape of the conduction band populated by cooling carriers. Within a sub-picosecond timescale, the spectral weight associated with free carriers diminishes, while new, well-defined subbands at lower energies, attributable to excitonic states, emerge. To elucidate this process, we perform first-principles simulations based on the recently developed excitonic Bloch equations [32], which establish the phononic origin of exciton formation. The calculations show that the dynamics develops a pronounced bottleneck as carrier relaxation crosses over from a continuum of free-particle states to a discrete excitonic manifold. This crossover is highly nontrivial in two-dimensional transition-metal dichalcogenides because valley multiplicity gives rise to a dense manifold of optically bright and dark excitonic states of comparable energy [33]. Populating these states requires large-momentum phonon emission and spin-flip processes during carrier relaxation. Our findings indicate that intermediate excitonic states mediate the conversion from free carriers to bound excitons while maintaining a low population. This specific mechanism underlies the transient coexistence of free-carrier and low-energy excitonic states observed as distinct spectral signatures.

tr-ARPES of exciton phono-conversion

The tr-ARPES measurement for 1L-WSe_2 was carried out using a time-of-flight momentum microscope (ToF-MM) at 100 K under ultrahigh vacuum conditions, where the schematic is drawn in Fig. 1c, and the detail is described in the "Methods" part and Extended Data Fig. 1. Free carriers are optically injected on the conduction band (CB) from the valence band (VB) using a 3.1-eV pump pulse, which is ~ 1 eV above the energy gap E_g. The pump fluence used was 1.6 μJ/cm^2, corresponding to a photoexcited carrier density of 3.2×10^{11}cm^{-2}, which remains well below the Mott transition threshold to preserve excitonic stability [34–36]. A time-delayed 21.7-eV

probe pulse enables us to simultaneously capture both VB and CB as time-, energy-, and momentum-resolved photoemission spectra with $\sim$ 100 fs temporal resolution. Figure. 1d shows the experimentally obtained three-dimensional band structure (k_x, k_y, and E) of VB before time zero and theoretically calculated CB. The VB shows the negative parabolic dispersion at the Γ point and $K(K')$ points hexagonally placed on the edge of the first Brillouin zone (see also Extended Data Fig. 1c). CB minima (valleys) are located at K and Q points. The energy linewidth (FWHM) of the ARPES spectra was estimated to be $\sim$ 88 meV at the maximum of the VBs (see Extended Data Fig. 1b and e). This value is much less than the previously reported experiments for 1L-WSe_2 [37, 38], allowing us to clearly distinguish spectral contributions between CB and excitons, whose energy gap is typically a few hundred meV.

Non-resonant above-gap pump excitation generates a hot electron-hole (e-h) plasma. The e-h pairs initially redistribute within the respective band edges, then coalesce into bound excitons, and ultimately relax into the lowest energy exciton states (Fig. 2a-c). Here, we directly capture these electronic excitation and relaxation processes with tr-ARPES. Figure 2d displays a time-delay series of ARPES spectra around the CB energy level sliced along a $\Gamma \rightarrow K$ direction, including a Q valley. Although the excitation occurs within the K valley, intervalley scattering mediated by the emission of large-momentum phonons efficiently transfers carriers to the Q valleys already during the pumping process [25, 39], see Fig. 2d at delay $\tau = 0$ ps. The positive parabolic dispersions at K and Q valleys are attributed to the presence of hot carriers, almost following the calculated CB dispersion. Shortly after the pump pulse ends ($\tau = 0.2$ ps), free carriers accumulate near the band minima. At later time delay, around $\tau = 0.4$ ps, transitions into the lowest-lying energy levels become apparent as free carriers begin to coalesce into bound states (see also Extended Data Fig. 4). Furthermore, the negative parabolic dispersion at 1.0 ps also confirms that the lowest energy states arises from excitons (see Extended Data Fig. 3) [20, 38]. The high-resolution experimental spectra reveal the coexistence of free carriers and low-energy excitons, characterized by a progressive transfer of spectral weight from the conduction bands signal to the in-gap excitonic sidebands. This fundamental relaxation process terminates around $\tau = 1.0$ ps.

Real time simulations successfully reproduce the experimental tr-ARPES spectra (see Methods), confirming the coexistence of free carriers and excitons (Fig. 2e). As pointed out in Refs. [40–43], the ARPES signal from photoelectrons of momentum $\mathbf{k}$ forming excitons occurs at energy $\epsilon_{v,\mathbf{k}-\mathbf{Q}} + E_{\mathbf{Q}}$, where $\epsilon_{v,\mathbf{k}}$ denotes the VB energy and $E_{\mathbf{Q}}$ the energy of excitons with center-of-mass momentum $\mathbf{Q}$, and has an intensity proportional to the population $N_{\mathbf{Q}}$ of the corresponding exciton state. This implies that the selective population of bright excitons ($\mathbf{Q} = 0$) results in the appearance of valence-band replicas blue-shifted by the exciton energy (see Fig. 2b) [15, 40, 42, 44, 45], as recently demonstrated in photoexcited two-dimensional materials [38, 39]. The population of dark excitons with finite momentum $\mathbf{Q}$ gives rise to replicas that are not only blue shifted but also displaced in momentum space. The above-gap photoexcitation followed by relaxation populates a broad manifold of quasi-degenerate excitonic states [33]. Therefore, photoelectrons of same momentum $\mathbf{k}$ belong to excitons of different center-of-mass momentum (see Extended Data Fig. 5).

The method used to simulate the real-time dynamics of free carrier and exciton populations is the first principles excitonic Bloch equations (XBE) [32], as described in Methods. In the XBE e-h states with center-of-mass momentum $\mathbf{Q}$ are converted into exciton states with center-of-mass momentum $\mathbf{Q}'$ by emitting a phonon with momentum $\mathbf{Q} - \mathbf{Q}'$. Alternative pathways such as Coulomb-induced carrier-carrier scattering or Auger-like processes, which are known to become significant at higher carrier densities, are neglected. The agreement between theory and experiment in Fig. 2 unequivocally establishes phono-conversion as the dominant mechanism responsible for the formation of excitons.

The XBE provide further microscopic insights into the phono-conversion process. As electrons and holes approach the band edges, the dissipation of their excess energy shifts from transitions within a continuum of states to scattering into a discrete manifold of bound excitonic states. This transition severely restricts the available scattering phase space, resulting in a dynamical bottleneck during carrier relaxation, and ultimately manifesting as a marked carrier accumulation at the CB minima. Energy conservation, combined with the relatively small phonon energies compared to the exciton binding energy, implies that exciton formation proceeds through a relaxation cascade [26, 46, 47]. In this process, carriers sequentially relax along the descending energy landscape, ultimately populating the lowest-lying excitonic states at the high-symmetry points. Notably, the occupation of intermediate states remains low, which explains why higher-energy states (including the bright A exciton) are not visible from the ARPES signal.

We stress that the existence of a regime in which free carriers and excitons coexist has remained uncertain, as neither experiments nor theoretical calculations had previously been able to establish it. Figure 2 provides unambiguous evidence for such coexistence.

Phono-conversion timescale

We analyze the time- and energy-resolved evolution of free carriers and excitons at K and Q valleys, as shown in Fig. 3a-b, respectively (See details in Extended Data Fig. 2). Our results successfully distinguish two spectral peaks of CB and exciton energy levels at each time delay and valley. The energy levels of CB and exciton at K valley are at 2.06 eV (K_{CB}) and 1.75 eV (K_{X}), while those in the Q valley are at 2.16 eV (Q_{CB}) and 1.85 eV (Q_{X}). Energy difference between K and Q valleys is $\sim$ 100 meV. In addition, the exciton binding energy is estimated to be $\sim$ 310 meV. These values are consistent with previous literature and our theoretical calculation [33, 48], see Extended Data Fig. 5a. As detailed in Extended Data Fig. 5(b,c) the signal at K is predominantly attributed to electrons at K bound in spin-dark excitons with holes at K and momentum-dark excitons with holes at K'. Meanwhile, the signal at Q stems mainly from electrons at Q bound in momentum-dark excitons with holes at K and K'. The formation of spin-dark excitons requires spin-flip processes and, according to our simulations, their growth is delayed and slower than that of spin-bright excitons, see Extended Data Fig. 7. Nevertheless, the final populations of the two spin species is comparable, highlighting the crucial role of spin-flip scattering in shaping the final exciton distribution.

The measurements indicate that the colascence of e-h pairs into excitons initiates a few hundreds of femtoseconds after the pump excitation. In Fig. 3c, we evaluate the generation and relaxation dynamics of free carriers and excitons at K and Q valleys, extracted from Figs. 3a and b. First, free carriers are generated in the CBs and relax to the CB minima within $\sim$ 300 fs. Subsequently, these carriers bound into excitons within a timescale of up to $\sim$ 1 ps, consistent with optical-pump terahertz-probe experiments [6, 7, 28]. Finally, the excitons relax with a characteristic time constant of approximately 2 ps.

XBE simulations are reported in Fig. 3 and well reproduce the multiple characteristic timescales observed experimentally. The small discrepancy in the onset of exciton populations is due to a slightly lower photon energy used in the calculations (see Methods).

Dark excitons and lineshape asymmetry

The presence of multiple excitonic states leaves a distinct fingerprint in the photoemission lineshape, offering an additional benchmark for theory: a pronounced asymmetry in the energy distribution curves (EDCs) at both K and Q points, characterized by an extended tail towards lower energies, see Fig. 4a,b.

The asymmetry, which is absent under selective resonant excitation [20], is accurately reproduced by our simulated tr-ARPES spectra. The numerical analysis reveals that this feature is a general hallmark of a quasi-thermal exciton population, and it originates from the imbalance between the effective masses M_{x} and m_v of excitons and valence holes respectively – $M_{\mathrm{x}} \approx 2m_v$ in WSe_2 [49, 50]. Consider a photoelectron with momentum $\mathbf{k}$ at the high-symmetry point, say the K point. According to Extended Data Fig. 5b, the tr-ARPES signal arises from quasi-degenerate excitonic states with momenta $\mathbf{Q}$ around Γ and K, so that $E_{\mathbf{Q}} \approx E_{\Gamma/K} + \frac{q^2}{2M_{\mathrm{x}}}$ (where q is a small momentum). In both cases $\epsilon_{v\mathbf{k}-\mathbf{Q}} \approx \epsilon_{vK} - \frac{q^2}{2m_v}$, and therefore a signal at energies $\epsilon_{v\mathbf{k}-\mathbf{Q}} + E_{\mathbf{Q}} \approx \epsilon_{vK} + E_{\Gamma/K} + \frac{q^2}{2}(\frac{1}{M_{\mathrm{x}}} - \frac{1}{m_v}) \leq \epsilon_{vK} + E_{\Gamma/K}$ with intensity proportional to the exciton population $N_{\mathbf{Q}}$ is expected. Accordingly, the quasi-thermal distribution of excitons (Extended Data Fig. 4c) gives rise to a lineshape featuring a peak near $\epsilon_{vK} + E_{\Gamma/K}$, accompanied by a tail extending toward lower energies. A similar analysis can be carried out for the lineshape at the Q point, thus explaining the observed asymmetry in the EDCs (see also Extended Data Fig. 6).

Summary and conclusions

Previous experimental [22, 31] and theoretical [40, 42, 43] studies have clarified the spectral fingerprints of excitonic replicas in time-resolved ARPES. However, the dynamical coexistence of free carriers and excitons—and the microscopic timescale over which unbound e-h pairs coalesce into bound excitons—has remained inaccessible. Here, we provide the first direct, real-time observation of the phonon-mediated conversion of free electron–hole pairs into excitons, resolving the emergence of composite quasiparticles from their elementary constituents as it unfolds in time.

Our results establish phonon-assisted electron–hole coalescence as a dominant and experimentally resolvable pathway for exciton formation in low-dimensional materials. First-principles simulations based on the excitonic Bloch equations framework reveal that exciton formation proceeds through multiple, well-separated timescales, reflecting a hierarchy of phonon-driven processes. These include intervalley scattering and spin-flip transitions, which govern the selective population of excitonic valleys at distinct symmetry points in momentum space.

Altogether, our work establishes a powerful paradigm in which the combination of ultrafast spectroscopy and advanced theoretical modeling enables unprecedented insight into the role of bosonic interactions in driving emergent quantum phenomena in layered materials. Beyond advancing fundamental understanding, these findings offer critical and actionable knowledge for the rational design of next-generation opto-electronic and valleytronic devices that harness and control exciton dynamics at their most fundamental level.

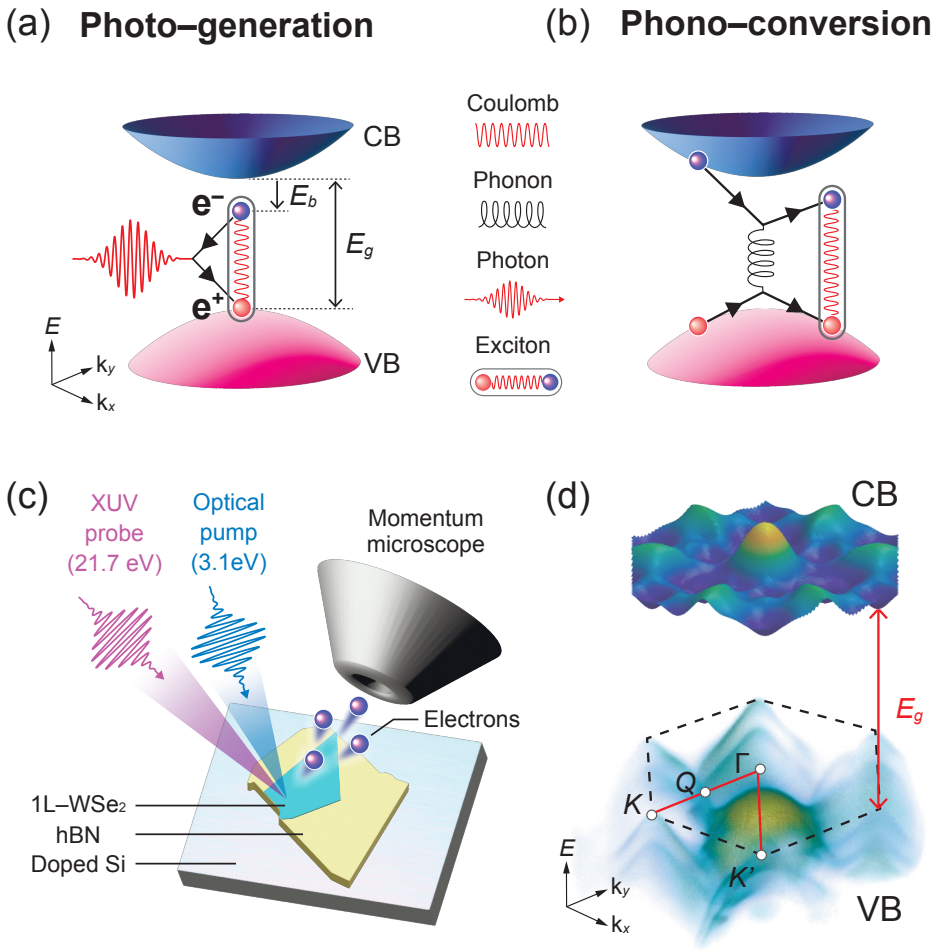

Fig. 1 Exciton phono-conversion dynamics and experimental setup. (a) Representation of the photo-generation process: an incoming photon (red pulse) with the same energy as the exciton is absorbed by an electron-hole pair to directly form a bound state. (b) Representation of the phono-conversion process: an electron in the conduction band (blue sphere) and a hole in the valence band (red sphere) emit a phonon (spring) and lower their energy by forming a bound exciton. (c) Experimental setup of tr-ARPES for a monolayer (1L) of WSe_2 on a hBN layer put onto a doped Si substrate. The 3.1 eV and 21.7 eV are used as the optical pump and XUV probe, respectively, with a time delay. Photoelectrons are collected by the objective lens of the momentum microscope, enabling us to analyze the energy and momentum dynamics in the sample. (d)Three-dimensional view of the valence band (VB) and conduction band (CB) of 1L-WSe_2 in the first Brillouin zone. The VB was measured by equilibrium ARPES. The CB was computed from first-principles calculations. The bandgap $E_g = 2.06$ eV corresponds to the energy difference between the VB maximum (VBM) and CB minimum (CBM) at the K valley of the first Brillouin zone.

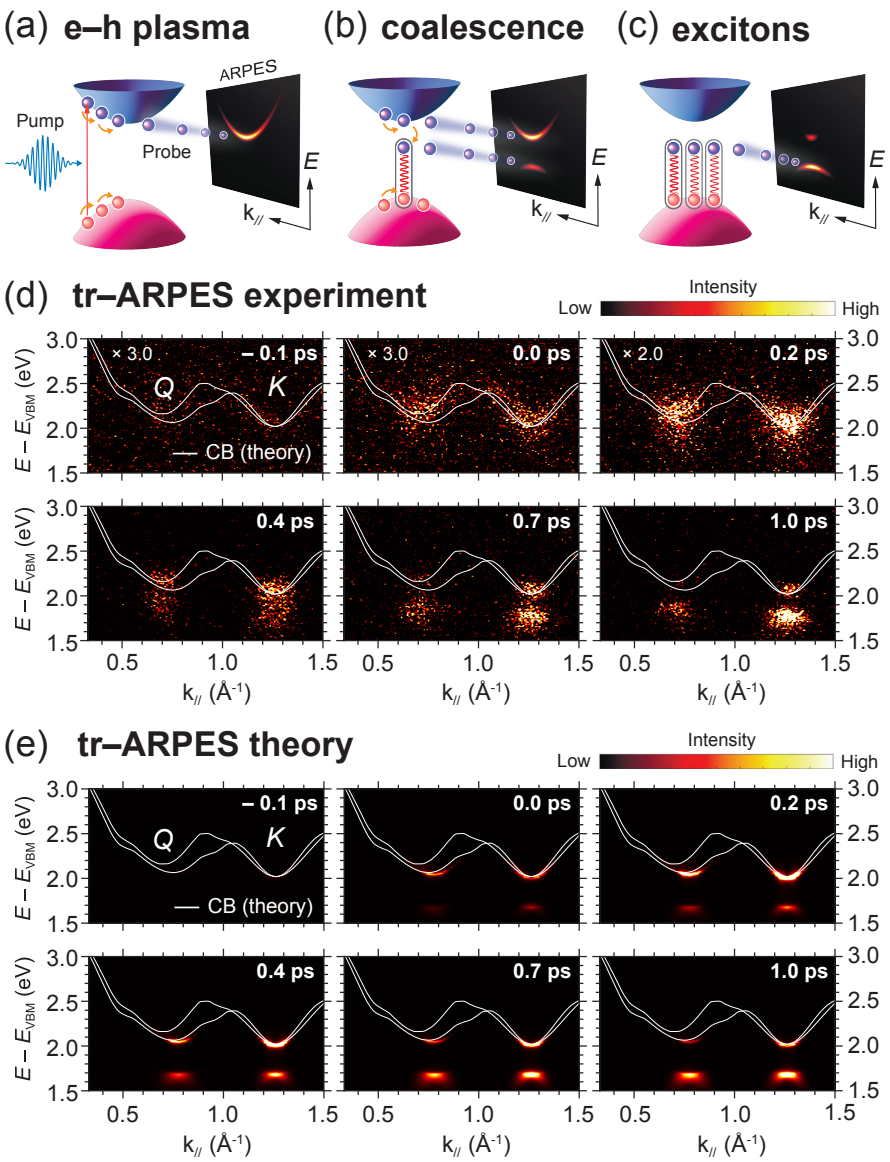

Fig. 2 Time-resolved ARPES in 1L-WSe_2. (a–c) Schematic view of exciton phono-conversion and its signatures in tr-ARPES: (a) Initial formation of an electron–hole plasma due to above-gap pumping and free-carrier relaxation toward the band edges, producing an ARPES signal that reflects the conduction band; (b) Coexistence of free carriers and bound excitons, giving rise to an additional excitonic sideband inside the gap; (c) Progressive coalescence of electron–hole pairs into excitons, resulting in a transfer of spectral weight from the conduction band signal to the in-gap excitonic sideband. (d) Experimental tr-ARPES data collected at different time delays from -0.1 to 1.0 ps (e) Calculated tr-ARPES spectra at the corresponding time delays. A small energy broadening $\eta = 0.01$ eV is used to resolve the dispersion of the excitonic sidebands. In all ARPES spectra, the energy E is measured with respect to the VBM: $E - E_{\mathrm{VBM}}$. In the panels corresponding to the delay $= -0.1$ ps, the ab-initio spin-resolved CB structure is overlaid as a dashed white line.

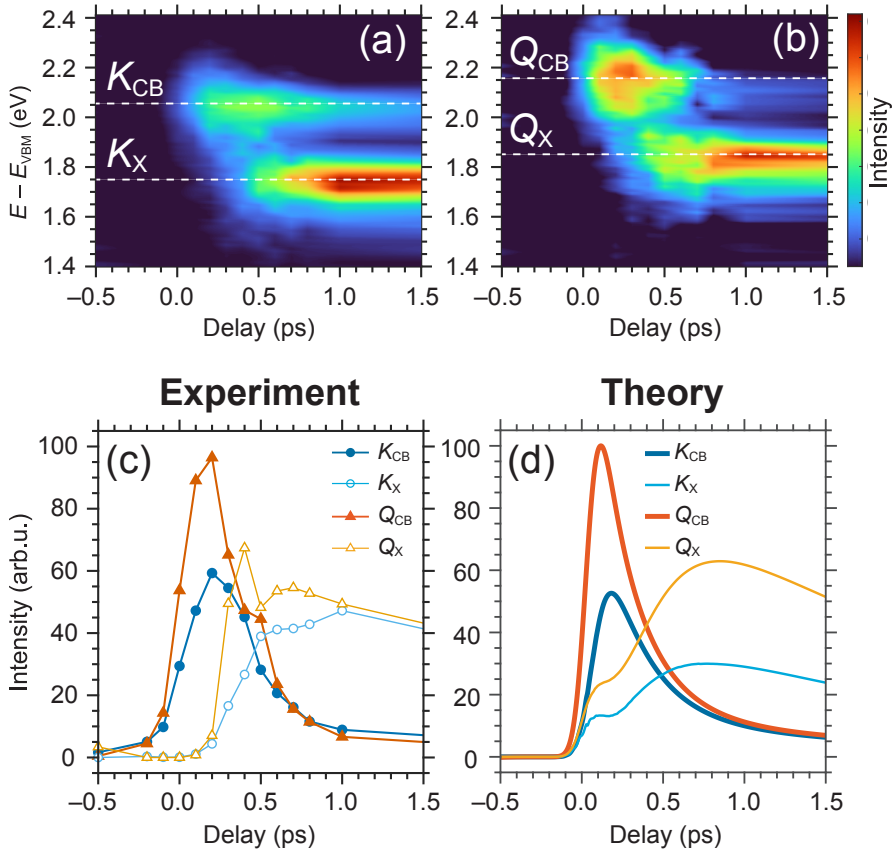

Fig. 3 Time evolution of transition from free carriers to excitons. The temporal energy evolution of photoelectron counts at the K valley (a) and the Q valley (b) extracted from the tr-ARPES measurement. The K_{CB} (2.06 eV) and Q_{CB} (2.16 eV) are the energy levels of CB at K and Q valleys, respectively. The K_X (1.75 eV) and Q_X (1.85 eV) are the excitonic levels at K and Q valleys, respectively. (c) The dynamics of photoelectron intensity at the energy levels of K_{CB}, Q_{CB}, K_X, and Q_X. extracted from (a) and (b). Connecting lines are guides to the eye. (d) Simulated tr-ARPES signal, processed identically to the experimental data in (c). Here, we have multiplied all curves by an exponential damping function with a lifetime of $\tau \approx 2$ ps [51], accounting for the electron-hole recombination that attenuates the quantities reported in panel (c).

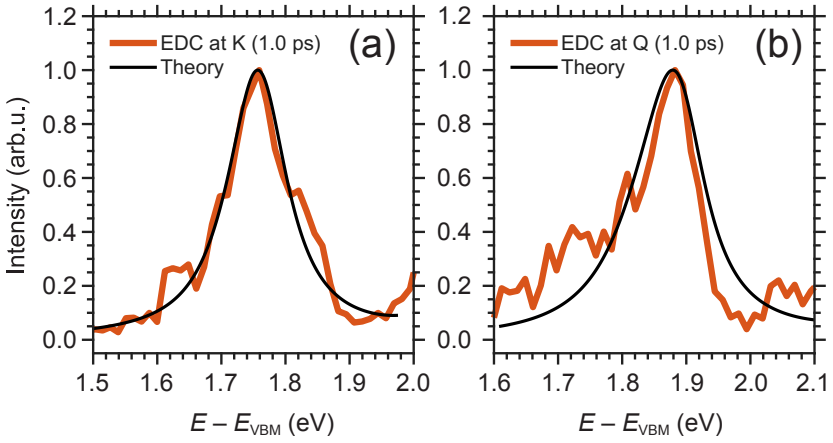

Fig. 4 Asymmetry of lineshape at exciton peaks. Comparison of energy distribution curves (EDCs) around the exciton peaks between experimental and theoretical tr-ARPES data at 1.0 ps at the K valley (a) and Q valley (b). The experimental EDCs are extracted by integrating the ARPES signal within a momentum window of 0.037 Å^{-1} × 0.037 Å^{-1} centered at the K and Q valleys. Overlaid theoretical EDCs are obtained using the same integration procedure, computed with an energy broadening parameter $\eta = 0.05$ eV.

Methods

Sample preparation. Monolayer(1L-) WSe_2 flakes were exfoliated from the bulk crystal (hqGraphene) onto a Si/SiO_2 substrate at the Quantum Material Press (QPress) facility in the Center for Functional Nanomaterials (CFN) at Brookhaven National Laboratory (BNL). Flakes of hexagonal boron nitride (hBN) were exfoliated from the bulk crystals (National Institute for Material Science, Japan) onto an n-doped silicon substrate. The monolayer flake was picked up from the Si/SiO_2 substrate and transferred on the top of the hBN flake using polycarbonate-based dry transfer technique, as shown in Extended Data Fig. 1(a) and (b). The size of 1L-WSe_2 flake is estimated to be approximately 15 μm $\times$ 20 μm. The sample was annealed in ultrahigh vacuum ($\sim 10^{-10}$ mbar) condition at 450 °C for 30 minutes.

Experimental set-up. The time-resolved ARPES experiment was carried out using a time-of-flight momentum microscope (ToF-MM, METIS1000, SPECS GmbH) combined with a home-built table-top high-harmonic generation (HHG) setup as an extreme ultraviolet (XUV) source, which has been described in detail in our previous work [20]. We used a Yb-doped fiber laser operating at 2 MHz with 230-fs pulse width. The laser system delivered a pulse energy of 50 μJ for 1030 nm, which was then split into 35 μJ for XUV generation as an ARPES probe pulse and 15 μJ for a non-collinear optical parametric amplifier (NOPA) to change the wavelength of the pump pulse. For the XUV generation, 35 μJ (1030 nm) was frequency doubled by a LiB_3O_5 (LBO) crystal to generate $\sim$ 15 μJ (515 nm). The 515-nm light was then focused on a Kr gas jet to generate the 21.7-eV XUV probe. The XUV probe was finally collected and focused onto the sample inside the microscope using an ellipsoidal mirror. For the pump excitation, we used a NOPA system to generate a 400-nm (3.1-eV) pulse. The ToF-MM collected the photoemitted electrons from the sample using immersion objective lens under the XUV-probe irradiation conditions. A 10-μm field aperture was inserted at the image plane in the ToF-MM to collect photoelectrons from a clean monolayer region (Extended Data Fig. 1(b)). The energy and momentum resolutions of the microscope were < 30 meV and < 0.01 Å^{-1}, respectively. All the ARPES experiments were performed at 100 K under ultrahigh vacuum conditions ($\sim 10^{-10}$ mbar).

Data analysis. Our measurement provides three dimensional (3D) photoemission intensity data (Energy, k_x and k_y). After correcting the distortion, we performed the analysis based on the corrected 3D data. All the photoemission spectra were normalized by the total photoemission signal of the valence bands of 1L-WSe_2 to compensate the variations in experimental integration time and photoemission yield. Extended Data Fig. 1(c) shows the momentum image in valence band region ($E - E_{\mathrm{VBM}} = -0.40$ eV) before pump (-0.5 ps). K points in a hexagonal pattern and Γ point at the center can be seen. ARPES spectrum was obtained by cutting the 3D data along the Γ-K direction, as shown in Extended Data Fig. 1(d). The linewidth (FWHM) at the valence band maximum (VBM) is estimated to be 88 meV by the gaussian fitting (Extended Data Fig. 1(e)). To extract the population of free carriers in the conduction band and the excitons, the photoemission intensity weas integrated within a 0.23 Å^{-1} $\times$ 0.23 Å^{-1} square region centered at K valley and Q valley to

get EDC between 1.2 eV to 3.0 eV, as shown in Extended Data Fig. 2. Two distinct peaks attributed to the conduction band free carriers and excitons can be clearly resolved. The background (red line) is approximated by asymmetric least squares from the EDC before optical excitation (-0.5 ps data). After background subtraction, the spectra were fitted using a two-Gaussian model to separate the contribution from the conduction-band carriers (blue shaded region) and excitons (red shaded region). The overall fit (grey line) including the background shows good agreement with the EDC (blue markers). The populations of carriers and excitons were quantified from the area under the respective fitted curve.

First-principle simulations. The nonequilibrium dynamics of carriers and excitons following laser excitation, including relaxation mediated by phonon emission, are simulated from first principles using the recently developed excitonic Bloch equations (XBE) [32]. These equations describe the temporal evolution of the occupations $N_{\lambda\mathbf{Q}}$ of all electron-hole (e-h) states in the system, including both quasi-free e-h pairs and bound excitons. Here $\mathbf{Q}$ denotes the center-of-mass momentum of the e-h state, and λ labels the corresponding branch. The XBE formulation is based on two key concepts. First, the occupation $N_{\lambda\mathbf{Q}}$ is decomposed into a coherent and an incoherent contribution

$$N_{\lambda\mathbf{Q}} = \delta_{\mathbf{Q},\mathbf{0}} N^{\mathrm{coh}}_{\lambda} + N^{\mathrm{inc}}_{\lambda\mathbf{Q}} \tag{1}$$

which obey distinct equations of motion. The coherent component is given by the square-modulus of the e-h polarization $N^{\mathrm{coh}}_{\lambda} = |\rho_{\lambda}|^2$, and is nonzero only for optically active bright states with zero momentum. Second, the evaluation of both ρ_{λ} and $N^{\mathrm{inc}}_{\lambda\mathbf{Q}}$ requires the explicit calculation of the occupations of *irreducible* e-h states [52] $\widetilde{N}_{\lambda\mathbf{Q}}$. These occupations enter the XBE as auxiliary dynamical variables and are essential to avoid overscreening effects, ensuring a consistent treatment of many-body interactions. The resulting XBE read [32]

$$\begin{aligned}
\frac{d}{dt}\rho_{\lambda} &= -iE_{\lambda\mathbf{0}}\rho_{\lambda} - i\Omega_{\lambda} - \frac{1}{2}\sum_{\widetilde{\lambda}'\mathbf{Q}} \left[\widetilde{\Gamma}^{\mathrm{pol}}_{\lambda\widetilde{\lambda}'\mathbf{Q}} + \widetilde{\Gamma}_{\lambda\widetilde{\lambda}'\mathbf{Q}}\widetilde{N}_{\widetilde{\lambda}'\mathbf{Q}}\right]\rho_{\lambda} \\
\frac{d}{dt}\widetilde{N}_{\widetilde{\lambda}\mathbf{Q}} &= -\widetilde{\Gamma}^{\mathrm{out}}_{\widetilde{\lambda}\mathbf{Q}}\widetilde{N}_{\widetilde{\lambda}\mathbf{Q}} + \widetilde{\Gamma}^{\mathrm{in}}_{\widetilde{\lambda}\mathbf{Q}}\left(1+\widetilde{N}_{\widetilde{\lambda}\mathbf{Q}}\right) \\
\frac{d}{dt}N^{\mathrm{inc}}_{\lambda\mathbf{Q}} &= -\Gamma^{\mathrm{out}}_{\lambda\mathbf{Q}}N^{\mathrm{inc}}_{\lambda\mathbf{Q}} + \Gamma^{\mathrm{in}}_{\lambda\mathbf{Q}}\left(1+N^{\mathrm{inc}}_{\lambda\mathbf{Q}}\right) + \sum_{\lambda'\widetilde{\lambda}} |S^{\mathbf{Q}}_{\lambda\widetilde{\lambda}}|^2 \left[\widetilde{\Gamma}^{\mathrm{pol}}_{\lambda'\widetilde{\lambda}\mathbf{Q}} + \widetilde{\Gamma}_{\lambda'\widetilde{\lambda}\mathbf{Q}}\widetilde{N}_{\widetilde{\lambda}\mathbf{Q}}\right]|\rho_{\lambda'}|^2
\end{aligned} \tag{2}$$

In the above equations $E_{\lambda\mathbf{Q}}$ is the energy of the e-h states, obtained from the solution of the Bethe-Salpeter equation (BSE)

$$(\epsilon_{c\mathbf{k}+\mathbf{Q}} - \epsilon_{v\mathbf{k}})A^{\lambda\mathbf{Q}}_{cv\mathbf{k}} - \sum_{c'v'\mathbf{k}'} K^{\mathrm{HSEX},\mathbf{Q}}_{cv\mathbf{k},c'v'\mathbf{k}'} A^{\lambda\mathbf{Q}}_{c'v'\mathbf{k}'} = E_{\lambda\mathbf{Q}}A^{\lambda\mathbf{Q}}_{cv\mathbf{k}}, \tag{3}$$

with $\epsilon_{v(c)\mathbf{k}}$ the valence (conduction) band dispersion, K^{HSEX} the Hartree plus screened-exchange (HSEX) kernel, and $A^{\lambda\mathbf{Q}}$ the e-h wavefunction. The discrete sector of the BSE spectrum describes bound excitonic states, while the continuum corresponds to unbound, quasi–free e-h pairs. The quantity $S^{\mathbf{Q}}$ denotes the overlap between

the wavefunctions $A^{\lambda\mathbf{Q}}$ obtained from Eq. (3) and the wavefunctions of irreducible p-h states. The latter are computed by solving an analogous BSE equation, in which the HSEX kernel is replaced by the screened-exchange one [52]. The laser-induced driving force $\Omega_\lambda = \sum_{cv\mathbf{k}} A^{\lambda\mathbf{0}}_{cv\mathbf{k}} \Omega_{cv\mathbf{k}}$ is determined by the Rabi frequencies $\Omega_{cv\mathbf{k}}$ corresponding to vertical transitions from valence states $v\mathbf{k}$ to the conduction states $c\mathbf{k}$. The XBE include also several rates describing distinct phonon-mediated processes. These comprise the polarization-decay ($\widetilde{\Gamma}^{\mathrm{pol}}$), and inelastic phonon-assisted transitions between e-h states. The latter accounts for both the depletion of a given e-h state, through out-scattering processes (Γ^{out}, $\widetilde{\Gamma}^{\mathrm{out}}$) and its increasing population via in-scattering processes (Γ^{in}, $\widetilde{\Gamma}^{\mathrm{in}}$, $\widetilde{\Gamma}$). These rates are determined by the overlap of electron–hole wavefunctions, modulated by the corresponding electron–phonon matrix elements, and are constrained by energy conservation during the scattering process. Explicit expressions for all rates are provided in the Supplementary Information.

Based on the occupations $N_{\lambda\mathbf{Q}}(\tau)$ given by the XBE, the time-resolved ARPES signal associated with photoelectrons of energy ϵ emitted by a probe pulse with central photon energy ω_0 at pump-probe delay τ can be expressed as [41]

$$I_{\mathbf{k}}(\tau,\epsilon) \propto \sum_{\lambda\mathbf{Q}} N_{\lambda\mathbf{Q}}(\tau) \sum_v \Big| \sum_c A^{\lambda\mathbf{Q}}_{cv\mathbf{k}-\mathbf{Q}} \Big|^2 \delta(\epsilon_{v\mathbf{k}-\mathbf{Q}} + E_{\lambda\mathbf{Q}} - \epsilon + \omega_0),$$

where, for simplicity, photoemission matrix elements have been neglected.

The single-particle band structure, phonon dispersions, electron–phonon couplings, and equilibrium excitonic properties of monolayer WSe_2 were computed following the methodology of Refs. [25, 41]. Within this framework, the energies and wavefunctions of irreducible e-h states coincide with those obtained from Eq. (3). Consequently, the exciton–phonon and irreducible-exciton–phonon couplings are identical. All quantities were evaluated and stored on a $\mathbf{k}$-grid of 3072 points sampling the first Brillouin zone. The electronic subspace was truncated to the two highest valence bands and the two lowest conduction bands, while the excitonic subspace was restricted to the ten lowest bound excitonic branches obtained from Eq. (3). To reduce memory requirements, the quasi-free e-h continuum eigenstates of Eq. (3) were approximated as $E_{\lambda\mathbf{Q}} \approx \epsilon_{c_\lambda \mathbf{k}+\mathbf{Q}} - \epsilon_{v_\lambda \mathbf{k}_\lambda}$, and $A^{\lambda\mathbf{Q}}_{cv\mathbf{k}} \approx \delta_{c,c_\lambda}\delta_{v,v_\lambda}\delta_{\mathbf{k},\mathbf{k}_\lambda}$. In the simulations, we explicitly included the lowest 200 e-h bands in the continuum sector, spanning energies up to 2.7 eV (approximately ~ 0.7 eV above than the bandgap). Exciton–phonon couplings were stored on a coarser $\mathbf{k}$-grid of 192 points and interpolated on-the-fly onto the denser grid during the time-dependent simulations.

We initialize the system in thermal equilibrium at $T = 100$ K, by setting $\rho_\lambda = N_{\lambda\mathbf{Q}} = \widetilde{N}_{\lambda\mathbf{Q}} = 0$. The dynamics are triggered by illuminating the system with a ~ 250 fs pump pulse lineraly polarized along the x direction, with above-gap central frequency ~ 2.4 eV, and of sufficiently low intensity to generate an excitation density $\sim 10^{11}$ cm^{-2}. The XBE are integrated using a fourth-order Runge-Kutta solver with time-step of 0.1 fs.

Supplementary information

0.1 Scattering rates

In this Section, we detail the evaluation of the scattering rates entering the XBE introduced in the Methods. The relevant ingredients are the phonon frequencies $\omega_{\alpha\mathbf{Q}}$, phonon occupation numbers $n_{\alpha\mathbf{Q}}$, electron-phonon (e-p) matrix elements, and the energies and wavefunctions of electron–hole (e–h) states. We adopt the convention that the e–p coupling $g^{\mu\mu'}_{\alpha-\mathbf{Q}}(\mathbf{k})$ describes the amplitude for an electron with momentum $\mathbf{k}$ to be scattered from band μ to band μ' by the phonon mode α with momentum $\mathbf{Q}$. Electron–hole eigenmodes are obtained by solving the Bethe–Salpeter equation (BSE)

$$(\epsilon_{c\mathbf{k}+\mathbf{Q}} - \epsilon_{v\mathbf{k}})A^{\lambda\mathbf{Q}}_{cv\mathbf{k}} - \sum_{c'v'\mathbf{k}'} K^{\mathrm{HSEX},\mathbf{Q}}_{cv\mathbf{k},c'v'\mathbf{k}'} A^{\lambda\mathbf{Q}}_{c'v'\mathbf{k}'} = E_{\lambda\mathbf{Q}} A^{\lambda\mathbf{Q}}_{cv\mathbf{k}}, \tag{4}$$

where $\epsilon_{v(c)\mathbf{k}}$ denotes the valence (conduction) band dispersion, and $A^{\lambda\mathbf{Q}}$ is the e-h wavefunction associated with eigen-energy $E_{\lambda\mathbf{Q}}$. The interaction kernel $K^{\mathrm{HSEX},\mathbf{Q}}_{cv\mathbf{k},c'v'\mathbf{k}'} = W_{c\mathbf{k}+\mathbf{Q}\,v'\mathbf{k}'\,v\mathbf{k}\,c'\mathbf{k}'+\mathbf{Q}} - v_{c\mathbf{k}+\mathbf{Q}\,v'\mathbf{k}'\,c'\mathbf{k}'+\mathbf{Q}\,v\mathbf{k}}$ includes both the Hartree and screened-exchange contributions. Here, v denotes the bare Coulomb interaction, while W is the statically screened Coulomb interaction. Irreducible e–h states are instead obtained from a modified BSE

$$(\epsilon_{c\mathbf{k}+\mathbf{Q}} - \epsilon_{v\mathbf{k}})\widetilde{A}^{\lambda\mathbf{Q}}_{cv\mathbf{k}} - \sum_{c'v'\mathbf{k}'} K^{\mathrm{SEX},\mathbf{Q}}_{cv\mathbf{k},c'v'\mathbf{k}'} \widetilde{A}^{\lambda\mathbf{Q}}_{c'v'\mathbf{k}'} = \widetilde{E}_{\lambda\mathbf{Q}} \widetilde{A}^{\lambda\mathbf{Q}}_{cv\mathbf{k}}, \tag{5}$$

where the kernel retains only the screened-exchange contribution, i.e. $K^{\mathrm{SEX},\mathbf{Q}}_{cv\mathbf{k},c'v'\mathbf{k}'} = W_{c\mathbf{k}+\mathbf{Q}\,v'\mathbf{k}'\,v\mathbf{k}\,c'\mathbf{k}'+\mathbf{Q}}$. The quantities introduced above allow us to construct the exciton–phonon coupling matrix elements [43, 53]

$$\begin{aligned}\mathcal{G}^{\lambda\lambda'}_{\alpha-\mathbf{Q}'}(\mathbf{Q}) = &\sum_{c_1c_2v_1\mathbf{k}_1} A^{\lambda\mathbf{Q}*}_{c_1v_1\mathbf{k}_1} g^{c_1c_2}_{\alpha-\mathbf{Q}'}(\mathbf{k}_1+\mathbf{Q}) A^{\lambda'\mathbf{Q}-\mathbf{Q}'}_{c_2v_1\mathbf{k}_1} \\ &- \sum_{c_1v_1v_2\mathbf{k}_1} A^{\lambda\mathbf{Q}*}_{c_1v_1\mathbf{k}_1} g^{v_2v_1}_{\alpha-\mathbf{Q}'}(\mathbf{k}_1+\mathbf{Q}') A^{\lambda'\mathbf{Q}-\mathbf{Q}'}_{c_1v_2\mathbf{k}_1+\mathbf{Q}'}\end{aligned} \tag{6}$$

as well as the irreducible-exciton–phonon couplings [32]

$$\begin{aligned}\widetilde{\mathcal{G}}^{\tilde{\lambda}\lambda'}_{\alpha-\mathbf{Q}'}(\mathbf{Q}) = &\sum_{c_1c_2v_1\mathbf{k}_1} \widetilde{A}^{\tilde{\lambda}\mathbf{Q}*}_{c_1v_1\mathbf{k}_1} g^{c_1c_2}_{\alpha-\mathbf{Q}'}(\mathbf{k}_1+\mathbf{Q}) A^{\lambda'\mathbf{Q}-\mathbf{Q}'}_{c_2v_1\mathbf{k}_1} \\ &- \sum_{c_1v_1v_2\mathbf{k}_1} \widetilde{A}^{\tilde{\lambda}\mathbf{Q}*}_{c_1v_1\mathbf{k}_1} g^{v_2v_1}_{\alpha-\mathbf{Q}'}(\mathbf{k}_1+\mathbf{Q}') A^{\lambda'\mathbf{Q}-\mathbf{Q}'}_{c_1v_2\mathbf{k}_1+\mathbf{Q}'}.\end{aligned} \tag{7}$$

These effective couplings $\mathcal{G}$ ($\widetilde{\mathcal{G}}$) describe the amplitude for an e-h state in branch λ and center-of-mass momentum $\mathbf{Q}$ to scatter into a (irreducible) state in branch λ' and momentum $\mathbf{Q}-\mathbf{Q}'$ by exchanging a phonon in mode α. Once the exciton–phonon

couplings are known, the rates are evaluated according to [32]

$$
\begin{aligned}
\widetilde{\Gamma}^{\mathrm{pol}}_{\lambda\widetilde{\lambda}'\mathbf{Q}} &= 2\pi \sum_{\alpha} \frac{|\widetilde{\mathcal{G}}^{\widetilde{\lambda}'\lambda}_{\alpha-\mathbf{Q}}(\mathbf{Q})|^2}{2\omega_{\alpha\mathbf{Q}}} \Big[\delta(\widetilde{E}_{\widetilde{\lambda}'\mathbf{Q}} - E_{\lambda\mathbf{0}} + \omega_{\alpha\mathbf{Q}})(1+n_{\alpha-\mathbf{Q}}) + \delta(\widetilde{E}_{\widetilde{\lambda}'\mathbf{Q}} - E_{\lambda\mathbf{0}} - \omega_{\alpha\mathbf{Q}})n_{\alpha\mathbf{Q}}\Big].\\
\widetilde{\Gamma}_{\lambda\widetilde{\lambda}'\mathbf{Q}} &= 2\pi \sum_{\alpha} \frac{|\widetilde{\mathcal{G}}^{\widetilde{\lambda}'\lambda}_{\alpha-\mathbf{Q}}(\mathbf{Q})|^2}{2\omega_{\alpha\mathbf{Q}}} \Big[\delta(\widetilde{E}_{\widetilde{\lambda}'\mathbf{Q}} - E_{\lambda\mathbf{0}} + \omega_{\alpha\mathbf{Q}}) - \delta(\widetilde{E}_{\widetilde{\lambda}'\mathbf{Q}} - E_{\lambda\mathbf{0}} - \omega_{\alpha\mathbf{Q}})\Big]\\
\widetilde{\Gamma}^{\mathrm{out}}_{\widetilde{\lambda}\mathbf{Q}} &= 2\pi \sum_{\lambda'\alpha\mathbf{Q}'} \frac{\big|\widetilde{\mathcal{G}}^{\widetilde{\lambda}\lambda'}_{\alpha-\mathbf{Q}'}(\mathbf{Q})\big|^2}{2\omega_{\alpha\mathbf{Q}'}} \big(1+N^{\mathrm{inc}}_{\lambda'\mathbf{Q}-\mathbf{Q}'}\big)\\
&\quad\times \Big[\delta\big(E_{\lambda'\mathbf{Q}-\mathbf{Q}'} - \widetilde{E}_{\widetilde{\lambda}\mathbf{Q}} + \omega_{\alpha\mathbf{Q}'}\big)(1+n_{\alpha\mathbf{Q}'}) + \delta\big(E_{\lambda'\mathbf{Q}-\mathbf{Q}'} - \widetilde{E}_{\widetilde{\lambda}\mathbf{Q}} - \omega_{\alpha\mathbf{Q}'}\big)n_{\alpha-\mathbf{Q}'}\Big],\\
\widetilde{\Gamma}^{\mathrm{in}}_{\widetilde{\lambda}\mathbf{Q}} &= 2\pi \sum_{\lambda'} \sum_{\mathbf{Q}'\alpha} \frac{\big|\widetilde{\mathcal{G}}^{\widetilde{\lambda}\lambda'}_{\alpha-\mathbf{Q}'}(\mathbf{Q})\big|^2}{2\omega_{\alpha\mathbf{Q}'}} N^{\mathrm{inc}}_{\lambda'\mathbf{Q}-\mathbf{Q}'}\\
&\quad\times \Big[\delta\big(E_{\lambda'\mathbf{Q}-\mathbf{Q}'} - \widetilde{E}_{\widetilde{\lambda}\mathbf{Q}} + \omega_{\alpha\mathbf{Q}'}\big)n_{\alpha\mathbf{Q}'} + \delta\big(E_{\lambda'\mathbf{Q}-\mathbf{Q}'} - \widetilde{E}_{\widetilde{\lambda}\mathbf{Q}} - \omega_{\alpha\mathbf{Q}'}\big)(1+n_{\alpha-\mathbf{Q}'})\Big].
\end{aligned}
\tag{8}
$$

The rates $\Gamma^{\mathrm{in/out}}$ have the same functional form as the corresponding irreducible rates $\widetilde{\Gamma}^{\mathrm{in/out}}$, with the irreducible exciton energies $\widetilde{E}$ and couplings $\widetilde{\mathcal{G}}$ replaced by the exciton energies E and couplings $\mathcal{G}$, respectively [32]. Both $\Gamma^{\mathrm{in/out}}$ and $\widetilde{\Gamma}^{\mathrm{in/out}}$ depend on the time-dependent state occupations $N^{\mathrm{inc}}_{\lambda'\mathbf{Q}}$ and must therefore be re-evaluated at each time step.

Data availability

The data supporting the findings of this study are available upon request.

Acknowledgements

E.P. and G.S. acknowledge funding from Ministero Università e Ricerca PRIN under grant agreement No. 2022WZ8LME, from INFN through project TIME2QUEST and from the Horizon Europe research and innovation program of the European Union under the Marie Skłodowska-Curie grant agreement 101118915 (TIMES). T.F. acknowledges support from the JSPS KAKENHI (Grant No. 25K17332) and Sasakawa Scientific Research Grant from the Japan Science Society (Grant No. 2024-2030). J.M. acknowledges support from the JSPS KAKENHI (Grant No. 24K00561). K.M.D acknowledges support from the JSPS KAKENHI (Grant Nos. 23K25807 and 24H00191) and JST FOREST program (Grant No. JPMJFR2230). J.N. acknowledges support from the NAWA Bekker Programme (Project No. BPN/BEK/2023/1/00009/DEC/1). This research used the Quantum material press (QPress) of the Center for Functional Nanomaterials (CFN), which is a U.S. Department of Energy Office of Science User Facility, at Brookhaven National Laboratory

under Contract No. DE-SC0012704. K.W. and T.T. acknowledge support from the JSPS KAKENHI (Grant Numbers 21H05233 and 23H02052), the CREST (Grant No. JPMJCR24A5), JST and World Premier International Research Center Initiative (WPI), MEXT, Japan.

Author contribution

T.F. and X.Z. performed the TR-ARPES measurements with the assistance of N.T., H.S., M.K.L.M. and J.M., and under the supervision of K.M.D. T.F., X.Z. and J.H. performed the analysis of the data under the supervision of K.M.D. E.P. and G.S. implemented the theoretical simulations. H.S., J.N., S.P., H.J., K.W. and T.T prepared the samples. E.P., G.S. and K.M.D. conceived and designed the study. All authors contributed to the writing and reviewing of the paper.

Competing interests

J.M., M.K.L.M. and K.M.D. are inventors on a granted patent related to this work filed by the Okinawa Institute of Science and Technology School Corporation (US patent 11,372,199). The authors declare no other competing interests.

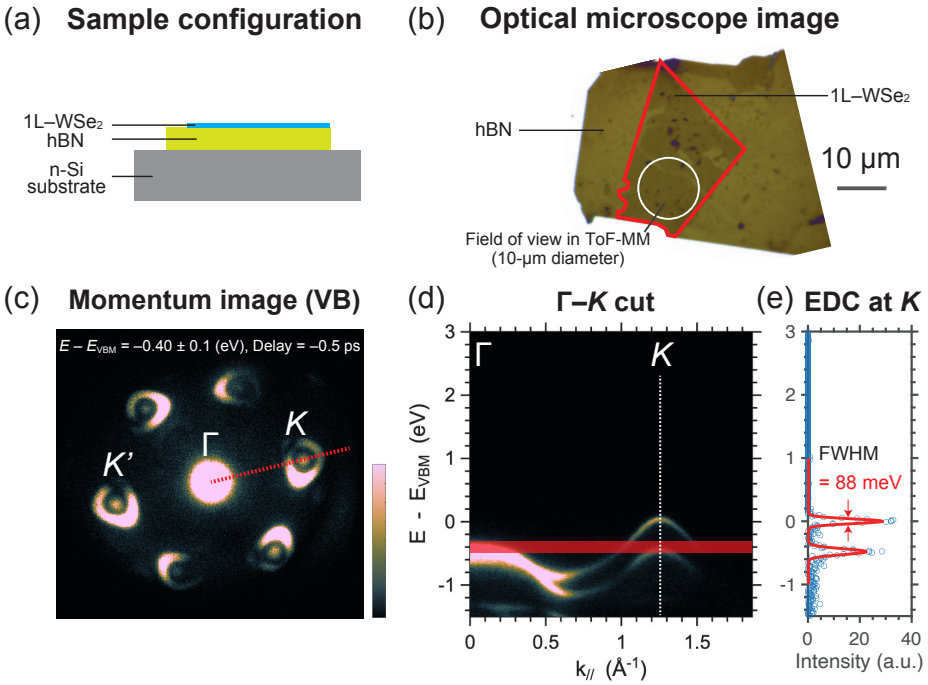

Extended Data Fig. 1 | Sample configurations and static tr-ARPES data of 1L–WSe_2 (a) Sample configuration of 1L–WSe_2 on hBN. (b) Optical microscope image of the sample. The brown area is hBN. The red marked area is 1L-WSe_2 on the hBN. The white circle denotes the field of view with 10-μm diameter during tr-ARPES measurements using the ToF-MM. (c) Momentum image of 1L-WSe_2 around valence band (VB) maximum at a negative time delay (-0.5 ps). The image was cut at $E - E_{\mathrm{VBM}} = -0.40$ eV integrated by ± 0.1 eV, which is shown in the red shaded area in (d). K points are located in a hexagonal pattern. Γ point is at center. (d) Static ARPES spectrum along Γ-K direction (red dashed line in (c)). (e) Energy distribution curve (EDC) at K point with the VB fit using gaussian functions. The EDC is extracted by integrating 0.022 Å$^{-1} \times 0.022$ Å^{-1} square region in momentum space centered at the K point. Linewidth (FWHM) of the top of VB was estimated to be 88 meV.

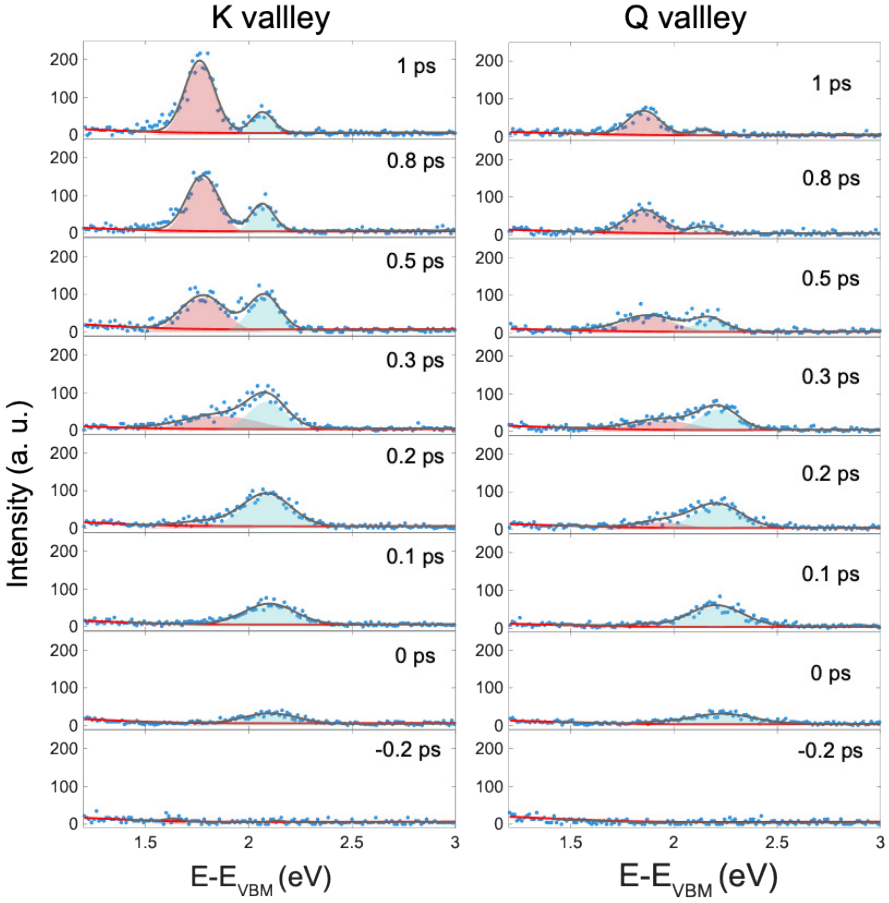

Extended Data Fig. 2 | Extracting population dynamics of conduction bands and excitons To extract the population dynamics, EDCs for each delay was extracted by integrating 0.23 $Å^{-1} \times 0.23$ $Å^{-1}$ square region centered at K and Q valleys in momentum space. Two gaussian fitting functions nicely caught two distinct peaks od conduction bands and excitons for each valley. Areas of the photoemission counts are plotted as population dynamics in Fig. 3(c).

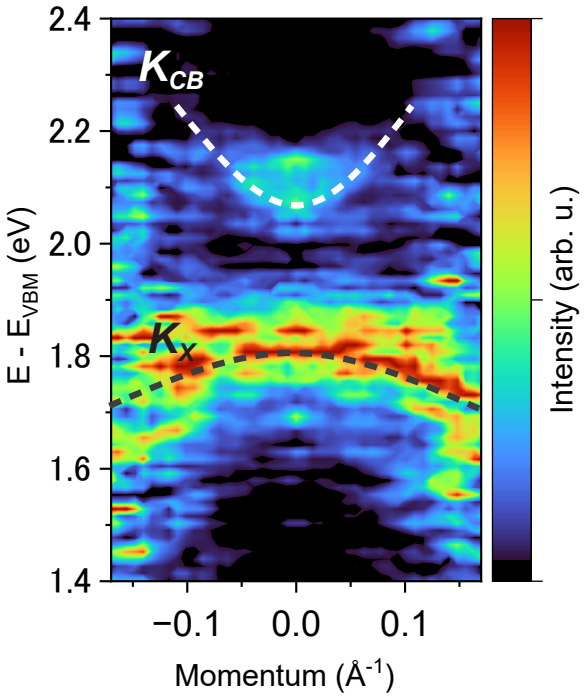

Extended Data Fig. 3 | Dispersion of the conduction band and exciton at K valley at 1.0 ps Two distinct peaks, as shown in Extended Data Fig.2, have energy dispersions in momentum space. White and black dashed lines are guide for the eyes. The conduction band K_{CB} shows positive dispersion, which is more prominent at earlier time delays (see Fig. 2(d)). The exciton K_{X} shows negative dispersion, which is obviously seen at the later time delay when the spectrum comes to have a minimum broadening effect.

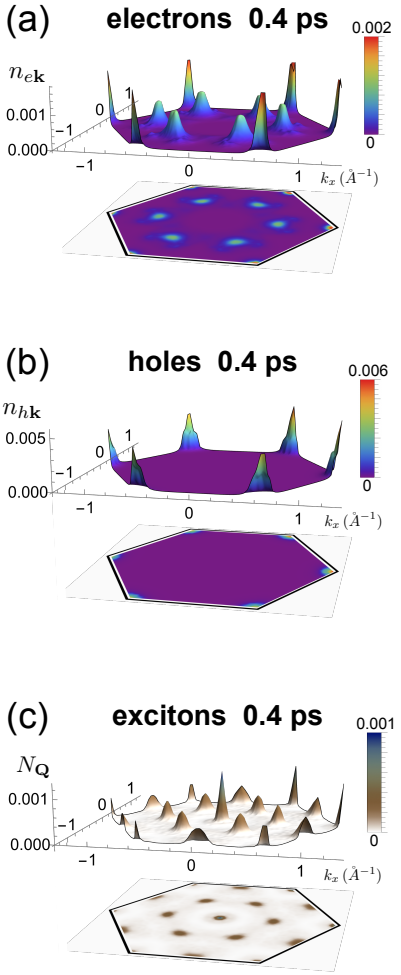

Extended Data Fig. 4 | Momentum-resolved electronic and excitonic populations at coalescence. (a) Electron distribution $n_{e\mathbf{k}}$, (b) hole distribution $n_{h\mathbf{k}}$, and (c) exciton distribution $N_{\mathbf{Q}}$ calculated across the entire first Brillouin zone at time delay $\tau = 0.4$ ps. At this stage, the e-h plasma has largely dissipated its excess kinetic energy. Further relaxation of the electronic subsystem occurs predominantly through exciton formation. Panel (c) shows a quasi-thermal distribution of excitons around the high-symmetry points Γ, K, Q, M. Since all these excitons are formed with valence holes located in either the K or K' valleys, the prominent ARPES signal comes from photoelectron with momenta $\mathbf{k}$ near the K and Q points, see Extended Data Fig. 5. The spectra in Fig. 2d-e are consistent with this analysis.

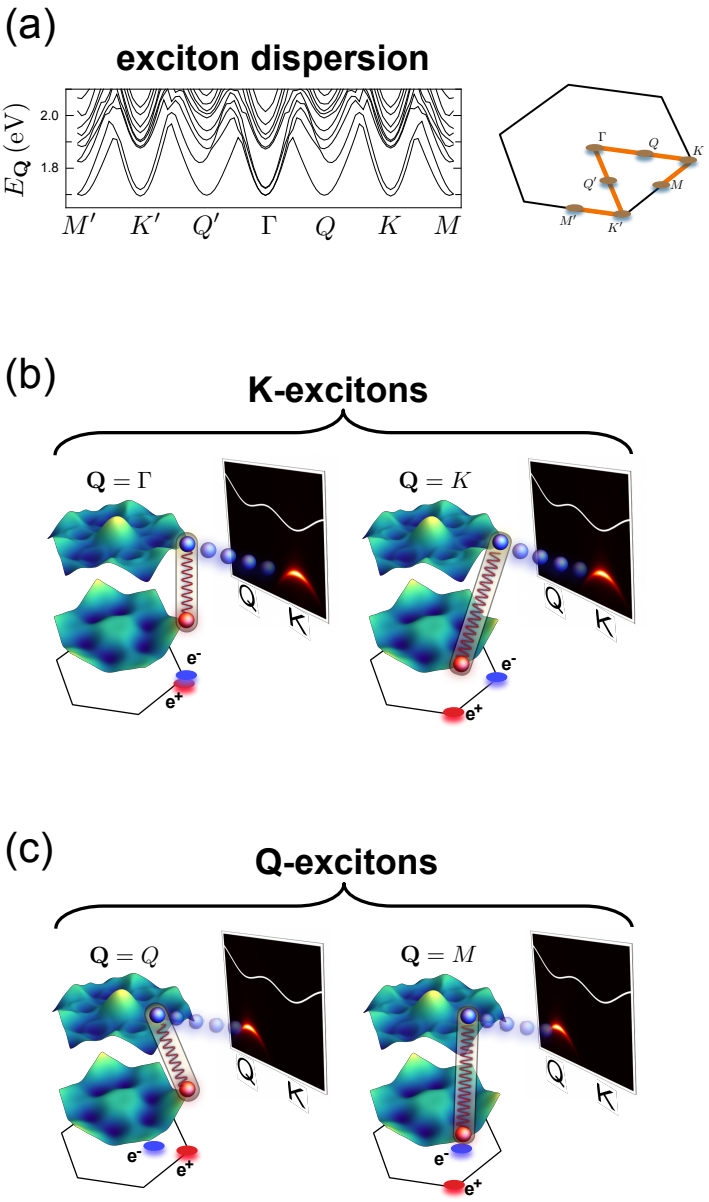

Extended Data Fig. 5 | Disentangling dark excitons contributions to ARPES signal. (a) Calculated low-energy exciton dispersion along a high-symmetry momentum path in the first Brillouin zone, as indicated in the inset. (b) Schematic illustration of the microscopic structure of the K-excitons, i.e. the excitonic states contributing to the ARPES signal near $\mathbf{k} = K$. These include direct excitons with center-of-mass momentum $\mathbf{Q} \approx \Gamma$ where both the electron and hole reside at the K point, and indirect excitons with $\mathbf{Q} \approx K$ composed of a hole at K' and an electron at K; (c) Same as (b), for the Q-excitons, which contribute to the ARPES signal near $\mathbf{k} = Q$. These are indirect excitons with $\mathbf{Q} \approx Q(M)$ comprising a hole at K (K') and an electron at Q. The signal observed at the K valley arises from a manifold of excitons having $\mathbf{Q}$ near the Γ and K points. Similarly, the signal observed at the Q valley stems from indirect excitons with $\mathbf{Q}$ near the Q and M points.

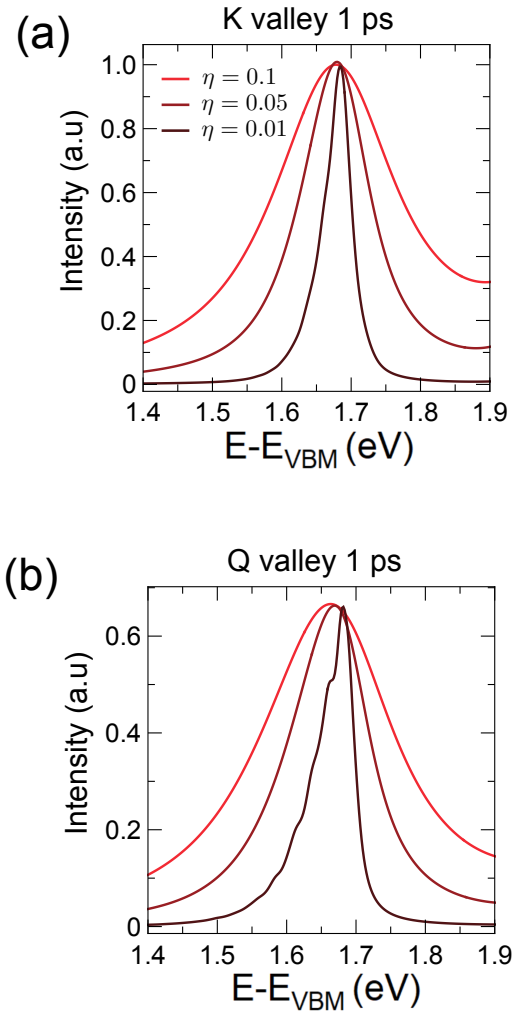

Extended Data Fig. 6 | Intrinsic nature of lineshape. (h-i) Theoretical analysis of the asymmetry in the EDCs at $\tau = 1$ ps for the K and Q valleys as a function of broadening parameter η varied between 0.01 eV and 0.1 eV. This analysis provides further evidence that the asymmetry of the EDC's is an intrinsic feature, and not an artifact of the experimental resolution. By reducing the broadening parameter the tail toward lower energies becomes increasingly more evident.

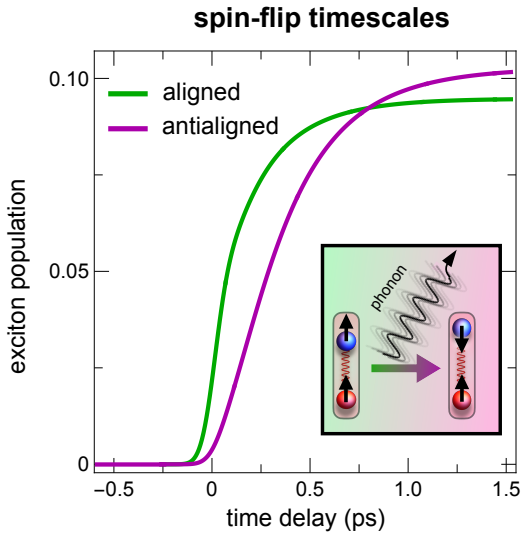

Extended Data Fig. 7 | Spin flip scattering. Simulated temporal evolution of the total population of spin-aligned (green curve) and spin-antialigned (violet curve) bound excitons. As the system evolves, excitons accumulate around the high-symmetry points. According to our Bethe–Salpeter equation (BSE) analysis, and consistent with previous reports [33, 47], the lowest-energy excitons around K and Q exhibit spin-aligned character while those around Γ and M are spin-antialigned. Since photoexcitation only generates spin-aligned electron–hole pairs, the formation of spin-antialigned excitons requires spin-flip processes, which in WSe_2 are primarily mediated by the emission of E'' optical phonons [54]. As a result, the population of spin-antialigned excitons (mainly from Γ and M) emerges at later times and grows more slowly than that of spin-aligned excitons (mainly from K and Q). Nevertheless, the populations of the two spin species become comparable within ∼1 ps.

References

[1] Mourzidis, K. et al. Exciton formation in two-dimensional semiconductors. Phys. Rev. X **15**, 031078 (2025). URL https://link.aps.org/doi/10.1103/66rj-jbqw.

[2] Kumar, R. et al. Exciton formation and relaxation dynamics in quantum wires. Phys. Rev. Lett. **81**, 2578–2581 (1998). URL https://link.aps.org/doi/10.1103/PhysRevLett.81.2578.

[3] Szczytko, J. et al. Determination of the exciton formation in quantum wells from time-resolved interband luminescence. Phys. Rev. Lett. **93**, 137401 (2004). URL https://link.aps.org/doi/10.1103/PhysRevLett.93.137401.

[4] Trovatello, Chiara and Katsch, Florian and Borys, Nicholas J. and Selig, Malte and Yao, Kaiyuan and Borrego-Varillas, Rocio and Scotognella, Francesco and Kriegel, Ilka and Yan, Aiming and Zettl, Alex and Schuck, P. James and Knorr, Andreas and Cerullo, Giulio and Dal Conte, Stefano. The ultrafast onset of

exciton formation in 2D semiconductors. Nature Communications **11**, 5277 (2020).

[5] Damen, T. C. et al. Dynamics of exciton formation and relaxation in gaas quantum wells. Phys. Rev. B **42**, 7434–7438 (1990). URL https://link.aps.org/doi/10.1103/PhysRevB.42.7434.

[6] Ceballos, F., Cui, Q., Bellus, M. Z. & Zhao, H. Exciton formation in monolayer transition metal dichalcogenides. Nanoscale **8**, 11681–11688 (2016). URL http://dx.doi.org/10.1039/C6NR02516A.

[7] Steinleitner, P. et al. Direct observation of ultrafast exciton formation in a monolayer of wse2. Nano Letters **17**, 1455–1460 (2017). URL https://doi.org/10.1021/acs.nanolett.6b04422.

[8] Eroglu, Z. E. et al. Ultrafast dynamics of exciton formation and decay in two-dimensional tungsten disulfide (2d-ws2) monolayers. Phys. Chem. Chem. Phys. **22**, 17385–17393 (2020). URL http://dx.doi.org/10.1039/D0CP03220D.

[9] Koch, S. W., Kira, M., Khitrova, G. & Gibbs, H. M. Semiconductor excitons in new light. Nature Materials **5**, 523–531 (2006). URL https://doi.org/10.1038/nmat1658.

[10] Wang, G. et al. Colloquium: Excitons in atomically thin transition metal dichalcogenides. Rev. Mod. Phys. **90**, 021001 (2018). URL https://link.aps.org/doi/10.1103/RevModPhys.90.021001.

[11] Wilson, N. P., Yao, W., Shan, J. & Xu, X. Excitons and emergent quantum phenomena in stacked 2d semiconductors. Nature **599**, 383–392 (2021). URL https://doi.org/10.1038/s41586-021-03979-1.

[12] Baranowski, M. & Plochocka, P. Excitons in metal-halide perovskites. Advanced Energy Materials **10**, 1903659 (2020). URL https://advanced.onlinelibrary.wiley.com/doi/abs/10.1002/aenm.201903659.

[13] Haug, H. Nonequilibrium many-body theory of optical nonlinearities of semiconductors. Journal of Luminescence **30**, 171–187 (1985). URL https://www.sciencedirect.com/science/article/pii/0022231385900511.

[14] Schmitt-Rink, S., Chemla, D. S. & Haug, H. Nonequilibrium theory of the optical stark effect and spectral hole burning in semiconductors. Phys. Rev. B **37**, 941–955 (1988). URL https://link.aps.org/doi/10.1103/PhysRevB.37.941.

[15] Perfetto, E., Sangalli, D., Marini, A. & Stefanucci, G. Pump-driven normal-to-excitonic insulator transition: Josephson oscillations and signatures of BEC-BCS crossover in time-resolved ARPES. Phys. Rev. Materials **3**, 124601 (2019). URL https://link.aps.org/doi/10.1103/PhysRevMaterials.3.124601.

[16] Sangalli, D. Excitons and carriers in transient absorption and time-resolved arpes spectroscopy: An ab initio approach. Phys. Rev. Mater. **5**, 083803 (2021). URL https://link.aps.org/doi/10.1103/PhysRevMaterials.5.083803.

[17] Rivera, P. et al. Valley-polarized exciton dynamics in a 2d semiconductor heterostructure. Science **351**, 688–691 (2016). URL https://www.science.org/doi/abs/10.1126/science.aac7820.

[18] Berghäuser, G. et al. Inverted valley polarization in optically excited transition metal dichalcogenides. Nature Communications **9**, 971 (2018). URL https://doi.org/10.1038/s41467-018-03354-1.

[19] Chan, Y.-H., Qiu, D. Y., da Jornada, F. H. & Louie, S. G. Giant self-driven exciton-floquet signatures in time-resolved photoemission spectroscopy of mos¡sub¿2¡/sub¿ from time-dependent gw approach. Proceedings of the National Academy of Sciences **120**, e2301957120 (2023). URL https://www.pnas.org/doi/abs/10.1073/pnas.2301957120.

[20] Pareek, V. et al. Driving floquet physics with excitonic fields. Nature Physics (2026). URL https://doi.org/10.1038/s41567-025-03132-z.

[21] Perfetto, E. & Stefanucci, G. Floquet topological phase of nondriven p-wave nonequilibrium excitonic insulators. Phys. Rev. Lett. **125**, 106401 (2020). URL https://link.aps.org/doi/10.1103/PhysRevLett.125.106401.

[22] Madéo, J. et al. Directly visualizing the momentum-forbidden dark excitons and their dynamics in atomically thin semiconductors. Science **370**, 1199–1204 (2020). URL https://www.science.org/doi/abs/10.1126/science.aba1029.

[23] Wallauer, R. et al. Momentum-resolved observation of exciton formation dynamics in monolayer ws2. Nano Letters **21**, 5867–5873 (2021). URL https://doi.org/10.1021/acs.nanolett.1c01839. PMID: 34165994.

[24] Caruso, F. Nonequilibrium lattice dynamics in monolayer mos2. The Journal of Physical Chemistry Letters **12**, 1734–1740 (2021). URL https://doi.org/10.1021/acs.jpclett.0c03616.

[25] Perfetto, E. & Stefanucci, G. Real-time GW-Ehrenfest-Fan-Migdal method for nonequilibrium 2d materials. Nano Letters **23**, 7029–7036 (2023). URL https://doi.org/10.1021/acs.nanolett.3c01772.

[26] Siantidis, K., Axt, V. M. & Kuhn, T. Dynamics of exciton formation for near band-gap excitations. Phys. Rev. B **65**, 035303 (2001). URL https://link.aps.org/doi/10.1103/PhysRevB.65.035303.

[27] Caruso, F. et al. The 2025 roadmap to ultrafast dynamics: frontiers of theoretical and computational modeling. Journal of Physics: Materials **9**, 012501 (2025).

URL https://doi.org/10.1088/2515-7639/ae1165.

[28] Cha, S. et al. 1s-intraexcitonic dynamics in monolayer mos2 probed by ultrafast mid-infrared spectroscopy. Nature Communications **7**, 10768 (2016). URL https://doi.org/10.1038/ncomms10768.

[29] Kaindl, R. A., Hägele, D., Carnahan, M. A. & Chemla, D. S. Transient terahertz spectroscopy of excitons and unbound carriers in quasi-two-dimensional electron-hole gases. Phys. Rev. B **79**, 045320 (2009). URL https://link.aps.org/doi/10.1103/PhysRevB.79.045320.

[30] Ménard, J. M. et al. Revealing the dark side of a bright exciton–polariton condensate. Nature Communications **5**, 4648 (2014). URL https://doi.org/10.1038/ncomms5648.

[31] Gosetti, V. et al. Unveiling exciton formation: exploring the early stages in time, energy and momentum domain. arXiv preprint arXiv:2412.02507 (2024).

[32] Stefanucci, G. & Perfetto, E. Excitonic Bloch equations from first principles. SciPost Phys. **18**, 009 (2025). URL https://scipost.org/10.21468/SciPostPhys.18.1.009.

[33] Deilmann, T. & Thygesen, K. S. Finite-momentum exciton landscape in mono- and bilayer transition metal dichalcogenides. 2D Materials **6**, 035003 (2019). URL https://dx.doi.org/10.1088/2053-1583/ab0e1d.

[34] Chernikov, A., Ruppert, C., Hill, H. M., Rigosi, A. F. & Heinz, T. F. Population inversion and giant bandgap renormalization in atomically thin WS_2 layers. Nature Photonics **9**, 466–470 (2015).

[35] Steinhoff, A. et al. Exciton fission in monolayer transition metal dichalcogenide semiconductors. Nat. Commun. **8**, 1166 (2017). URL https://doi.org/10.1038/s41467-017-01298-6.

[36] Dendzik, M. et al. Observation of an excitonic mott transition through ultrafast core-cum-conduction photoemission spectroscopy. Phys. Rev. Lett. **125**, 096401 (2020). URL https://link.aps.org/doi/10.1103/PhysRevLett.125.096401.

[37] Madéo, J. et al. Directly visualizing the momentum forbidden dark excitons and their dynamics in atomically thin semiconductors. arXiv preprint arXiv:2005.00241 (2020).

[38] Man, M. K. L. et al. Experimental measurement of the intrinsic excitonic wave function. Science Advances **7**, eabg0192 (2021). URL https://www.science.org/doi/abs/10.1126/sciadv.abg0192.

[39] Dong, S. et al. Direct measurement of key exciton properties: Energy, dynamics, and spatial distribution of the wave function. Natural Sciences **1**, e10010 (2021). URL https://onlinelibrary.wiley.com/doi/abs/10.1002/ntls.10010.

[40] Perfetto, E., Sangalli, D., Marini, A. & Stefanucci, G. First-principles approach to excitons in time-resolved and angle-resolved photoemission spectra. Phys. Rev. B **94**, 245303 (2016). URL https://link.aps.org/doi/10.1103/PhysRevB.94.245303.

[41] Stefanucci, G. & Perfetto, E. Unified first-principles formula for time-resolved arpes spectra of coherent and incoherent excitons (2026). URL https://arxiv.org/abs/2601.16786. 2601.16786.

[42] Rustagi, A. & Kemper, A. F. Photoemission signature of excitons. Phys. Rev. B **97**, 235310 (2018). URL https://link.aps.org/doi/10.1103/PhysRevB.97.235310.

[43] Chen, H.-Y., Sangalli, D. & Bernardi, M. Exciton-phonon interaction and relaxation times from first principles. Phys. Rev. Lett. **125**, 107401 (2020). URL https://link.aps.org/doi/10.1103/PhysRevLett.125.107401.

[44] Perfetto, E., Bianchi, S. & Stefanucci, G. Time-resolved arpes spectra of nonequilibrium excitonic insulators: Revealing macroscopic coherence with ultrashort pulses. Phys. Rev. B **101**, 041201 (2020). URL https://link.aps.org/doi/10.1103/PhysRevB.101.041201.

[45] Christiansen, D., Selig, M., Malic, E., Ernstorfer, R. & Knorr, A. Theory of exciton dynamics in time-resolved arpes: Intra- and intervalley scattering in two-dimensional semiconductors. Phys. Rev. B **100**, 205401 (2019). URL https://link.aps.org/doi/10.1103/PhysRevB.100.205401.

[46] Brem, S., Selig, M., Berghaeuser, G. & Malic, E. Exciton relaxation cascade in two-dimensional transition metal dichalcogenides. Scientific Reports **8**, 8238 (2018). URL https://doi.org/10.1038/s41598-018-25906-7.

[47] Chen, H.-Y., Sangalli, D. & Bernardi, M. First-principles ultrafast exciton dynamics and time-domain spectroscopies: Dark-exciton mediated valley depolarization in monolayer wse_2. Phys. Rev. Res. **4**, 043203 (2022). URL https://link.aps.org/doi/10.1103/PhysRevResearch.4.043203.

[48] Lin, K.-Q. et al. Narrow-band high-lying excitons with negative-mass electrons in monolayer wse2. Nature Communications **12**, 5500 (2021). URL https://doi.org/10.1038/s41467-021-25499-2.

[49] Kormányos, A. et al. Corrigendum: k.p theory for two-dimensional transition metal dichalcogenide semiconductors (2015 2d mater. 2 022001). 2D Materials **2**, 049501 (2015). URL https://dx.doi.org/10.1088/2053-1583/2/4/049501.

[50] Shih, Y.-C., Nilsson, F. A. & Guo, G.-Y. Electron energy loss spectra and exciton band structure of wse_2 monolayers studied by ab initio bethe-salpeter equation calculations. Phys. Rev. B **110**, 205417 (2024). URL https://link.aps.org/doi/10.1103/PhysRevB.110.205417.

[51] Robert, C. et al. Exciton radiative lifetime in transition metal dichalcogenide monolayers. Phys. Rev. B **93**, 205423 (2016). URL https://link.aps.org/doi/10.1103/PhysRevB.93.205423.

[52] Paleari, F. & Marini, A. Exciton-phonon interaction calls for a revision of the "exciton" concept. Phys. Rev. B **106**, 125403 (2022). URL https://link.aps.org/doi/10.1103/PhysRevB.106.125403.

[53] Antonius, G. & Louie, S. G. Theory of exciton-phonon coupling. Phys. Rev. B **105**, 085111 (2022). URL https://link.aps.org/doi/10.1103/PhysRevB.105.085111.

[54] Zhang, X.-W. & Cao, T. Ab initio calculations of spin-nonconserving exciton–phonon scattering in monolayer transition metal dichalcogenides. Journal of Physics: Condensed Matter **34**, 264002 (2022). URL https://dx.doi.org/10.1088/1361-648X/ac6649.